Available online at www.sciencedirect.com
ScienceDirect
Planetary and Space Science 56 (2008) 3–18
Planetary and Space Science
www.elsevier.com/locate/pss

Ion and neutral sources and sinks within Saturn's *inner* magnetosphere: Cassini results

E.C. Sittler Jr.[a,*], N. Andre[b], M. Blanc[c], M. Burger[a], R.E. Johnson[d], A. Coates[e], A. Rymer[f], D. Reisenfeld[g], M.F. Thomsen[h], A. Persoon[i], M. Dougherty[j], H.T. Smith[d], R.A. Baragiola[d], R.E. Hartle[a], D. Chornay[a], M.D. Shappirio[a], D. Simpson[a], D.J. McComas[k], D.T. Young[k]

[a]*NASA/Goddard Space Flight Center, MD, USA*
[b]*ESTEC, Noordjwick, Netherlands*
[c]*Centre d'Etudes Spatiales des Rayonnements (CESR), Toulouse, France*
[d]*University of Virginia, Charlottesville, VA, USA*
[e]*Mullard Space Science Laboratory, UK*
[f]*Johns Hopkins Applied Physics Laboratory, MD, USA*
[g]*University of Montana, MT, USA*
[h]*Los Alamos National Laboratory, NM, USA*
[i]*University of Iowa, Iowa City, IA, USA*
[j]*Blackett Laboratory, Imperial College, London, UK*
[k]*Southwest Research Institute, San Antonio, TX, USA*

Received 7 March 2007; received in revised form 26 April 2007; accepted 11 June 2007
Available online 20 September 2007

Abstract

Using ion–electron fluid parameters derived from Cassini Plasma Spectrometer (CAPS) observations within Saturn's inner magnetosphere as presented in Sittler et al. [2006a. Cassini observations of Saturn's inner plasmasphere: Saturn orbit insertion results. Planet. Space Sci., 54, 1197–1210], one can estimate the ion total flux tube content, $N_{ION}L^2$, for protons, H^+, and water group ions, W^+, as a function of radial distance or dipole L shell. In Sittler et al. [2005. Preliminary results on Saturn's inner plasmasphere as observed by Cassini: comparison with Voyager. Geophys. Res. Lett. 32(14), L14S04), it was shown that protons and water group ions dominated the plasmasphere composition. Using the ion–electron fluid parameters as boundary condition for each L shell traversed by the Cassini spacecraft, we self-consistently solve for the ambipolar electric field and the ion distribution along each of those field lines. Temperature anisotropies from Voyager plasma observations are used with $(T_\perp/T_\parallel)_{W^+}\sim5$ and $(T_\perp/T_\parallel)_{H^+}\sim2$. The radio and plasma wave science (RPWS) electron density observations from previous publications are used to indirectly confirm usage of the above temperature anisotropies for water group ions and protons. In the case of electrons we assume they are isotropic due to their short scattering time scales. When the above is done, our calculation show $N_{ION}L^2$ for H^+ and W^+ peaking near Dione's L shell with values similar to that found from Voyager plasma observations. We are able to show that water molecules are the dominant source of ions within Saturn's inner magnetosphere. We estimate the ion production rate $S_{ION}\sim10^{27}$ ions/s as function of dipole L using N_{H^+}, N_{W^+} and the time scale for ion loss due to radial transport τ_D and ion–electron recombination τ_{REC}. The ion production shows localized peaks near the L shells of Tethys, Dione and Rhea, but not Enceladus. We then estimate the neutral production rate, S_W, from our ion production rate, S_{ION}, and the time scale for loss of neutrals by ionization, τ_{ION}, and charge exchange, τ_{CH}. The estimated source rate for water molecules shows a pronounced peak near Enceladus' L shell $L\sim4$, with a value $S_W\sim2\times10^{28}$ mol/s.

Keywords: Saturn; Magnetosphere; Plasmasphere; Plasma; Magnetic fields; Ion-neutral sources

*Corresponding author. Tel.: +1 301 2869215; fax: +1 301 2861433.
E-mail address: Edward.C.Sittler@nasa.gov (E.C. Sittler Jr.).

0032-0633/$ - see front matter © 2007 Elsevier Ltd. All rights reserved.
doi:10.1016/j.pss.2007.06.006

1. Introduction

Using Voyager 1 and 2 plasma observations Richardson and Sittler (1990) presented the first 2D maps of the ion–electron densities within Saturn's magnetosphere and computed such quantities as the ion total flux tube content $N_{ION}L^2$ within Saturn's inner magnetosphere for dipole $L<12$. To do this, they used the ion–electron fluid parameters derived by Richardson (1986) and Sittler et al. (1983), respectively. Here, we repeat that effort using the ion–electron fluid parameters presented in Sittler et al. (2005, 2006a), using Cassini Plasma Spectrometer (CAPS) plasma observations acquired during the Saturn Orbit Insertion (SOI) approach trajectory ($3.4<L<10$). The advantage of this particular data set is that the instrument's field-of-view (FOV) is fixed (i.e., non-actuating), the instrument's FOV intersects the equatorial plane, and the instrument is operating at a high telemetry rate, ~8 kbp, with coincidence ion data. Therefore, we are able to sample the data with 32 s resolution or better, and the use of coincidence data is less susceptible to the contaminating effects of Saturn's penetrating radiation belt particles, the coupling within the instrument for protons and water group ions is less than 5% (i.e., 100% for non-coincidence singles data) and the coincidence ion data is less susceptible to the effects of scattering within the instrument (i.e., cross-talk effects). Furthermore, in the case of Cassini we have composition measurements which show protons and water group ions dominating the ion composition (Young et al., 2005; Sittler et al., 2005). The main disadvantage of this data set is that we must assume the temperature anisotropy of the ions and electrons. Here, we use the values inferred by Richardson and Sittler (1990). Sittler et al. (2005, 2006a) have also presented indirect evidence for our assumed ion temperature anisotropies, and further evidence is provided in this paper. We are in the process of measuring *in situ* the ion temperature anisotropies from later orbits within Saturn's inner magnetosphere when actuator motion was enabled and temperature anisotropies can be measured. This analysis is not yet complete.

In this paper, we solve for the ion densities of protons H^+ and water group ions W^+ (O^+, OH^+, H_2O^+, H_3O^+) along dipole field lines, by solving the field-aligned force balance equations with ambipolar electric field $E_{\parallel}$ as described in Maurice et al. (1997). We use the case of bi-Maxwellian distributions for both ions and electrons as a simplification of the Maurice et al. equations. The Maurice et al. (1997) results can also be applied to the more general case which includes ring current corrections to the magnetic field lines and the use of non-Maxwellian distributions for ions and electrons, such as kappa distributions or shell distribution for ions. We also derive approximate expressions for the neutral production and ion production as a function of dipole L, which can be used in the place of the self-consistent but more complex modeling done by Richardson et al. (1998). Our approach, which uses the radial transport timescales estimated by Richardson et al. (1998), is thus not self-consistent, but allows the physical concepts and parameterizations to be more easily realized. Due to instrument errors, uncertainties in our field-aligned extrapolations and uncertainties in various reaction rates, we consider our results accurate to within a factor of 2 in an absolute sense.

Cassini observations have revealed that the icy moon Enceladus is highly active with plumes or jets of water vapor and condensed water (i.e., dust particles) emanating from its south polar region (Porco et al., 2006; Hansen et al., 2006; Waite et al., 2006; Tokar et al., 2006; Brown et al., 2006; Spencer et al., 2006; Spahn et al., 2006; Dougherty et al., 2006; Jones et al., 2006). From these observations, Johnson et al. (2006) and Burger et al. (2007) have inferred the presence of a narrow neutral cloud of water vapor extending all around Saturn as a torus centered on Enceladus' L shell. Johnson et al. (2006) has shown that charge exchange reaction collisions between the rotating ions and this neutral water cloud will produce the neutral OH cloud originally discovered by Shemansky et al. (1993) using Hubble Space Telescope (HST) observations if the Enceladus source rate is $\sim 10^{28}$ mol/s. Burger et al. (2007) showed that Enceladus' plumes are consistent with emitting water molecules at the rate $S_W \sim 10^{28}$ mol/s, and Hansen et al. (2006) inferred a rate $\sim(0.5-1)\times 10^{28}$ mol/s using UVIS stellar occultation data at Enceladus and assumed ejecta speeds. Richardson et al. (1998) originally estimated a source rate $S_W \sim 10^{27}$ mol/s, but more recently, Jurac and Richardson (2005) estimate a source rate $S_W \sim 10^{28}$ mol/s. Our results provide an independent estimate of the neutral source term $S_W \sim 2\times 10^{28}$ mol/s, which supports the recent estimates.

A major finding of Cassini is that molecular water group ions dominate over atomic oxygen ions near Enceladus' L shell (Young et al., 2005) where electron temperatures $T_e \sim 1$ eV (Sittler et al., 2005, 2006a). Because of this, ion–electron recombination reaction time scales are very short within Saturn's inner magnetosphere, $\tau_{REC} \sim 2\times 10^5$ s, accounting for our higher neutral production rates $S_W \sim 10^{28}$ mol/s than originally estimated by Richardson et al. (1998), $S_W \sim 10^{27}$ mol/s, where atomic oxygen was thought to dominate. Our model is not self-consistent and we must use the neutral cloud model by Johnson et al. (2006), which includes both the Enceladus water cloud and the OH cloud or torus.

The outline of the paper is the introduction, followed by description of the 2D plasma density model of Saturn's plasmasphere and results, derivation of the equations used to estimate ion production rates and neutral production rates within Saturn's plasmasphere, results of ion–neutral production rate calculations, discussion section and conclusion section.

2. 2D ion density model of Saturn's plasmasphere

In this section, we present the field-aligned force balance equations derived by Maurice et al. (1997) in the limit of

a dipole magnetic field and assumed bi-Maxwellian distributions for the ions and electrons. This is a simplification of the more general case which includes ring current corrections and the possibility that the ion–electron particle distributions are not described by bi-Maxwellian velocity distribution functions (VDF). The equations are solved by using the ion–electron fluid parameters along the spacecraft trajectory as a boundary condition for our ion–electron density solutions along dipole field lines. We then show examples of our solutions for various dipole L values and then show 2D maps of the ion densities and electron densities for $3.4<L<10$. We provide fluid parameters in 2D for protons, H^+, water group ions, W^+, and electrons, which are derived from our solutions. When there are three or more species, which is the case here (i.e., H^+, W^+, e^-), we must solve the equations numerically. The equations are integrated using the IMSL Fortran routine DDASPG which uses the Petzold-Gear BDF Method for first-order differential-algebraic system of equations.

2.1. Ion–electron field-aligned dipole force balance equations

The basic equations as derived by Maurice et al. (1997) are as follows:

$$\sum_i Z_i n_i = 0 \text{ with } Z_i = +1 \;\&\; Z_e = -1, \tag{1a}$$

$$\frac{1}{n_i}\frac{dn_i}{ds} = \left(1-\frac{T_\perp}{T_\parallel}\right)_i \frac{1}{B}\frac{dB}{ds} - \frac{1}{kT_{\parallel i}}\frac{d\psi_i}{ds} \quad i = H^+, W^+, e^-, \tag{1b}$$

$$\frac{d\psi_i}{ds} = -q_i E_\parallel - m_i \frac{d}{ds}\left(\frac{1}{2}\Omega^2 R^2 + \frac{GM_s}{r}\right), \Omega = V_{\phi,\mathrm{obs}}/R, \tag{1c}$$

$$\left(\sum_j Z_j^2 \frac{n_j}{kT_{\parallel j}}\right) eE_\parallel = \left(\sum_j m_j Z_j \frac{n_j}{kT_{\parallel j}}\right) + \left(\sum_j n_j Z_j \frac{T_{\perp j}}{T_{\parallel j}}\right)\frac{1}{B}\frac{dB}{ds}. \tag{1d}$$

The first equation, Eq. (1a), enforces charge neutrality for all arc lengths, s, along a dipole field line L. Eq. (1b) is three separate equations for protons, water group ions and electrons. The above set of equations give the balance of forces along a dipole field line with the first term on the right being the magnetic mirror force, while the second term, as shown by Eq. (1c), includes the ambipolar electric field $E_\parallel$, centrifugal force and gravitational force, respectively. The last equation, Eq. (1d), gives the ambipolar electric field $E_\parallel$. Along the Cassini trajectory the spacecraft intersects a range of dipole L values ($3.4<L<10$), for which we have the fluid parameters, electron density, n_{ec}, electron perpendicular temperature, $T_{\perp e}$, proton density, n_{H^+}, proton perpendicular temperature, $T_{\perp H^+}$, water group ion density, n_{W^+}, water group ion perpendicular temperature, $T_{\perp W^+}$, cylindrical radial flow velocity, V_R, and azimuthal flow velocity, V_ϕ, at a particular (r, z) for each L value. The magnetic field magnitude is given by $B(s)$, Ω is the angular velocity of the flow, R is the cylindrical radius, m_i is the ion mass, G is the gravitational constant, e is the electric charge, $q_i = eZ_i$ and n_i is the ion or electron density. We then assume that $(T_\perp/T_\parallel)_{W^+} = 5$, $(T_\perp/T_\parallel)_{H^+} = 2$ and $(T_\perp/T_\parallel)_e = 1$ at equator for all L values. It is the ion–electron field-aligned temperatures, $T_{\parallel i}$, which determine the thickness of the plasmasphere relative to the ring plane. The assumed temperature anisotropies come from Richardson and Sittler (1990) and the indirect inferences by Sittler et al. (2005, 2006a). We show further observational evidence for the assumed ion–electron equatorial temperature anisotropies, by combining Cassini radio and plasma wave science (RPWS) UHR observations from Moncuquet et al. (2005) and Persoon et al. (2005, 2006), CAPS ion densities from Sittler et al. (2006a) and our 2D ion density solutions presented here. This is done in Section 2.3. The parallel component of the temperature, $T_{\parallel i}$, is assumed to be constant along dipole field lines and the perpendicular temperature $T_{\perp i}$ is assumed to obey the following relationship as described in Maurice et al. (1997) and Huang and Birmingham (1992) where the first adiabatic invariant is conserved:

$$kT_\parallel = kT_{||,\mathrm{eq}}, \tag{2a}$$

$$\frac{kT_{||}}{kT_\perp} = 1 - \frac{B_{\mathrm{eq}}}{B(s)}\left[1 - \frac{kT_{||,\mathrm{eq}}}{kT_{\perp,\mathrm{eq}}}\right]. \tag{2b}$$

This equation shows, for fixed L, that the ions and electrons become isotropic at high magnetic latitudes with $T_{\perp i} \to T_{\parallel i}$ as the latitude $\lambda \to \lambda_{\mathrm{iono}}$ where $\lambda_{\mathrm{iono}} \approx \pi/2$-arcsin $(1/\sqrt{L})$ is the latitude of the dipole field line at Saturn's ionosphere.

Sittler et al. (2005, 2006a) presented the thermal electron temperatures. As discussed in Rymer et al. (2006), the electron population is composed of thermal (cold) and suprathermal (hot) components. The cold component tends to dominate the electron density, while the suprathermal component may contribute significantly to the electron temperature. Both components, in general, will be important for electron impact ionization rates for neutrals. The cold component, especially when cold, $T_{ec} \sim 1$ eV, will be important for ion–electron recombination rates. For our field-aligned force balance calculations, it is most desirable to use both the thermal and suprathermal electron populations. Parameters for the separate populations are not yet available, but we do have estimates of the total electron temperature T_e which is shown in Fig. 1. As can be seen, the total electron temperatures for dipole L outside Dione's L shell, are significantly greater than those for the thermal electrons ($T_{ec} \sim 30$ eV and $T_e \sim 100$ eV at 1600 SCET for day 182 2004). At the Enceladus–Tethys transition region where $T_e \sim 1$–3 eV, the electron impact ionization rates can be a strong function of electron temperature. In this region the hot electrons will tend to dominate the ionization rates relative to the thermal electrons. In this

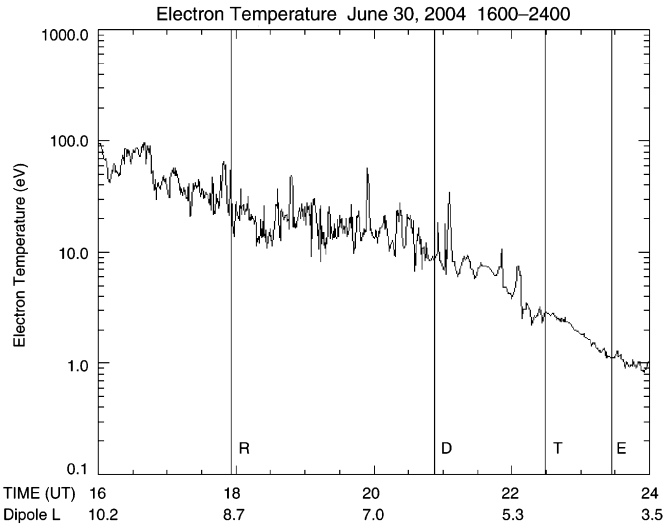

Fig. 1. Total electron temperature plotted as function of spacecraft event time (SCET). The satellite L shells are indicated, with M = Mimas, E = Enceladus, T = Tethys, D = Dione and R = Rhea.

inner region, T_e can be significantly contaminated by penetrating radiation and estimates of the hot electron component can be very uncertain. Tokar et al. (2006) did report hot electron densities N_{eh}~0.12 el/cm^3 and temperatures T_{eh}~12 eV during Cassini's close encounter with Enceladus on 14 July 2005. But, one would prefer parameters for SOI epoch and here we refer to the estimates by Moncuquet et al. (2005) who give T_{eh}~50 eV in the Enceladus–Tethys region, but give no hot electron density estimates. From Voyager 1 electron plasma observations reported by Sittler et al. (1983), they estimate T_{eh}~100 eV in the Enceladus–Tethys region. They also give hot electron densities N_{eh}~1.0 el/cm^3 at L~5.0 and N_{eh}~0.1 el/cm^3 at L~4.0. We use Voyager 1 outbound data when spacecraft is closest to ring plane. Both the Moncuquet et al. (2005) and Sittler et al. (1983) hot electron estimates are not contaminated by the effects of penetrating radiation. The Moncuquet et al. (2005) and Sittler et al. (1983) are reasonably close in hot electron temperature and the Tokar et al. (2006) hot electron temperatures may be low due to the spacecraft's close proximity to Enceladus. So, we choose the Moncuquet et al. (2005) results for T_{eh} since occurred during SOI epoch and use Sittler et al. (1983) results for N_{eh}. We then combine our SOI measured thermal electron densities and temperatures (i.e., single Maxwellian fits) from Sittler et al. (2006a) with the hot electron paprameters just noted, to compute total electron temperatures inside Tethys' L shell or $L<5.0$. Outside this distance, $L>5.0$, we use the moment estimated total electron temperatures noted above, which do include the hot electron component. The results are shown in Fig. 1 where we see a smooth transition at L~5.0, which indicates our estimates for T_e inside L~5.0 are approximately correct. For our calculations of T_e, we only use electron measurements for energies $E<1$ keV. This was done since most of the electron density is confined to the thermal electron population and most contributions to electron impact ionization rates of neutrals is confined to electron energies less than 1 keV. This approach also tends to minimize the effects of penetrating radiation.

2.2. 2D solutions of the ion–electron densities for Saturn's plasmasphere

The Cassini SOI trajectory approached Saturn at $\lambda\sim-12^\circ$, L~10 and then dipped toward the ring plane as it approached Saturn such that at L~3.4, $\lambda\sim-2^\circ$. After that time, at L~3.4 inbound, the CAPS Ion Mass Spectrometer (IMS) high voltage was turned off, in order to safe instrument during orbit insertion burn over Saturn's rings. In Figs. 2–4, we show solutions of the ion–electron densities along dipole field lines for L~10 (outside Rhea's L shell~8.74), 6.3 (Dione L shell) and 4.0 (~Enceladus L shell), respectively. The solution at L~10 was at sufficiently high latitude, $\lambda\sim-12^\circ$, where the proton densities approximately equaled the water group ion densities, $n_{h^+}\approx n_{W^+}$. At L~6.3, the spacecraft latitude $\lambda\sim-5^\circ$ was low enough that $n_{W^+}\gg n_{H^+}$ at the observation site. At L~4.0 the spacecraft is very near the ring plane, $\lambda\sim-2^\circ$, so that the proton densities are negligible relative to the water group ion densities, $n_{W^+}\gg n_{H^+}$. The solutions also show that protons dominate at high latitudes.

In Figs. 5–7, we show 2D contour maps of the proton densities, water group ion densities and electron densities, respectively. Dipole field lines are super-imposed. The 2D maps were derived from a continuum of solutions as shown in Figs. 2–4 as the spacecraft moved from L~10 to L~3.4. Fig. 5 shows the protons peaking off the equatorial plane, which is due to the field-aligned ambipolar electric field. The protons are significantly affected by the ambipolar

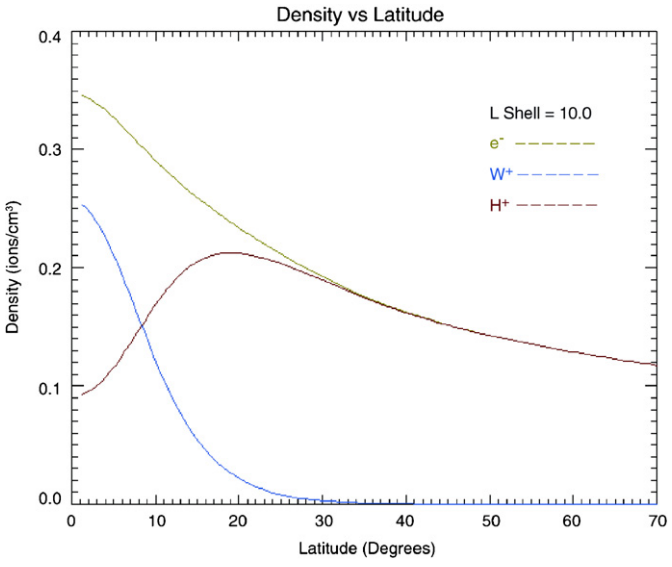

Fig. 2. Field-aligned solution of ion and electron densities plotted along dipole field line as function of latitude for $L=10$. H^+ density indicated in red, W^+ density indicated in blue and electron density indicated in green.

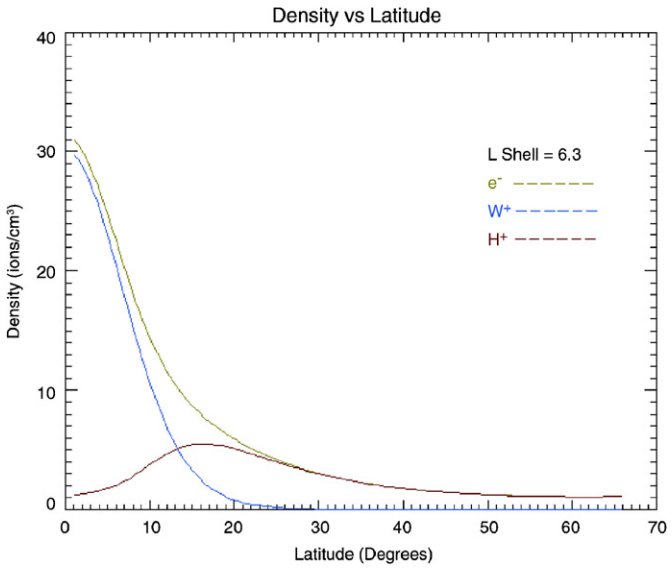

Fig. 3. Same as Fig. 2, except now at Dione's L shell with $L = 6.3$.

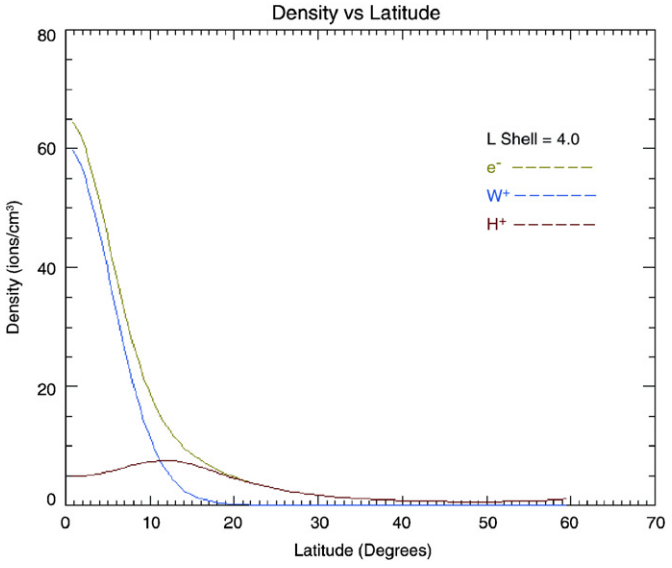

Fig. 4. Same as Fig. 2, except now near Enceladus' L shell with $L = 4.0$.

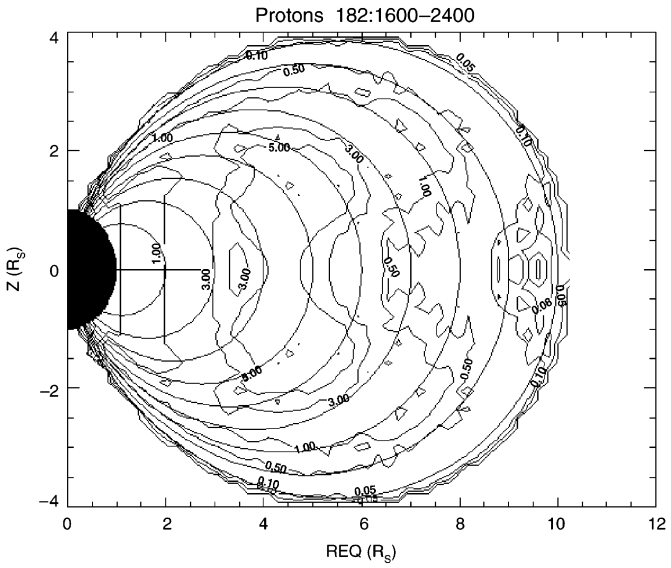

Fig. 5. 2D contour plot of proton density as function of equatorial radius R_{EQ} and vertical distance Z for Saturn-centered coordinate system. Dipole field lines super-imposed and contours labeled in cgs units or protons/cm^3.

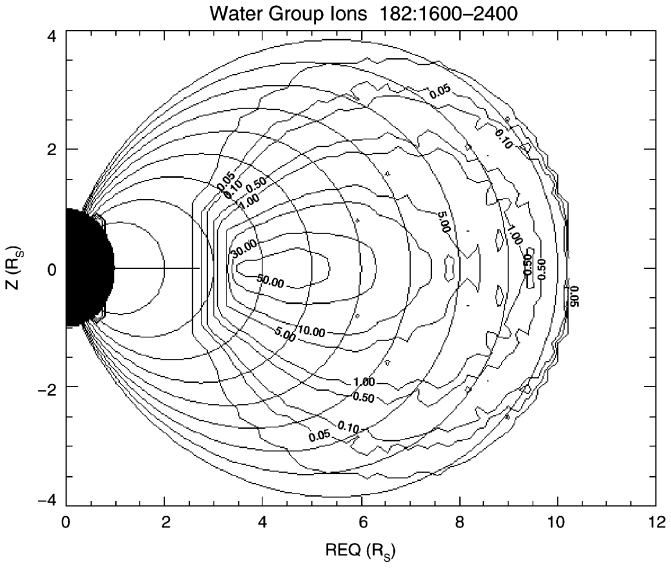

Fig. 6. Same as Fig. 5, except now we have 2D contour plots of water group ion density. Dipole field lines are super-imposed. Contours labeled in units of ions/cm^3.

electric field since, as shown in Sittler et al. (2006a) the proton temperature approximately equals the thermal electron temperature, $T_{H^+} \approx T_{ec}$. Furthermore, since the thermal proton temperature $T_{H^+} < T_e$ (total electron temperature), the field-aligned solutions for protons will be sensitive functions of electron temperature anisotropies; $(T_\perp/T_\parallel)_e > 1.0$ will confine protons nearer the equatorial plane while dumbbell distributions, $(T_\parallel/T_\perp)_e > 1.0$, will cause protons to move to higher latitudes. Fig. 6 shows the heavy water group ions being centrifugally confined near the equatorial plane for all L. Here, we note that if $(T_\perp/T_\parallel)_{W^+} \sim 1.0$, the water group ion density scale height would be ~3 times greater than derived here and violate observations (see Moncuquet et al., 2005). The electron density, $n_{ec} = n_{H^+} + n_{W^+}$ in Fig. 7 shows centrifugal confine of the plasma plus the presence of protons at higher latitudes. This can also be seen in Figs. 2–4. We are now in a position to numerically integrate along magnetic field lines to compute the total ion flux tube content $N_{ION}L^2$ for protons and water group ions.

As an example of what can also be achieved from such calculations, we show 2D maps of the plasma beta, $\beta = (n_e T_e + n_{H^+} T_{H^+} + n_{W^+} T_{W^+})/(B^2/8\pi)$, in Fig. 8 and the Alfven Mach number, $M_A = V_\phi/V_A$ with $V_A = B/\sqrt{4\pi\rho}$ the Alfven speed and $\rho = n_{H^+} m_{H^+} + n_{W^+} m_{W^+}$ the mass density of the plasma, in Fig. 9. The solutions show, that within the equatorial plane, the plasma beta can be

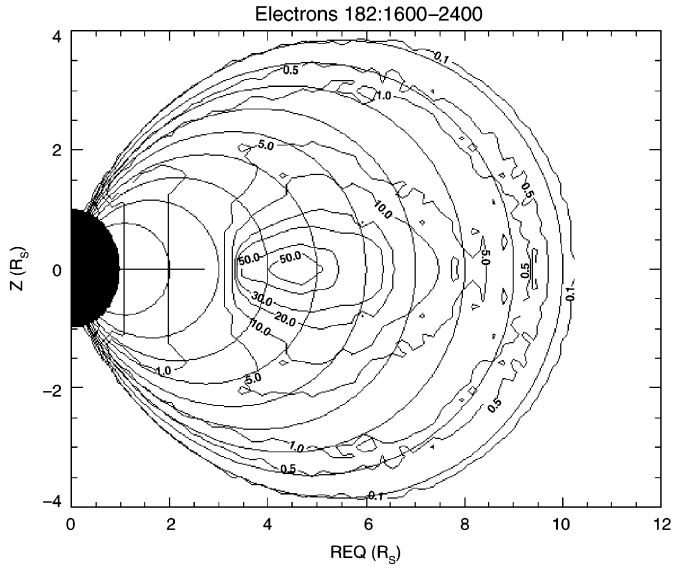

Fig. 7. Same as Fig. 5, except now we have 2D contour plots of electron density. Dipole field lines are super-imposed. Contours labeled in units of el/cm^3.

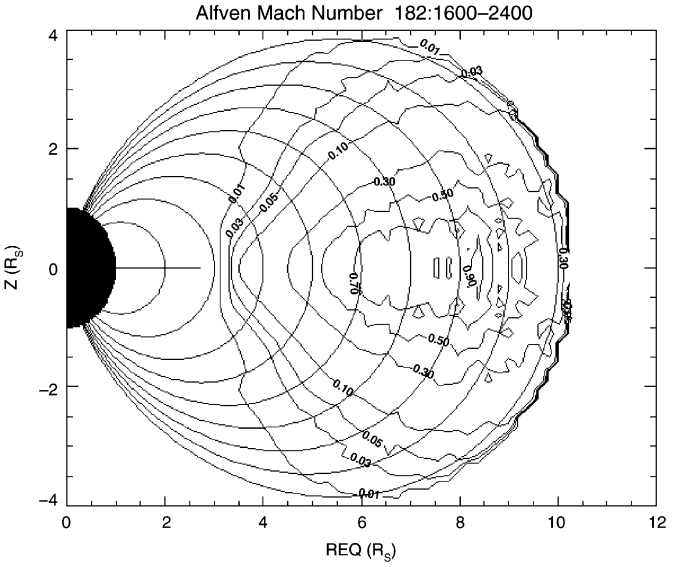

Fig. 9. Same as Fig. 8, except now we have 2D contour plots of Alfven Mach number M_A. Dipole field lines are super-imposed.

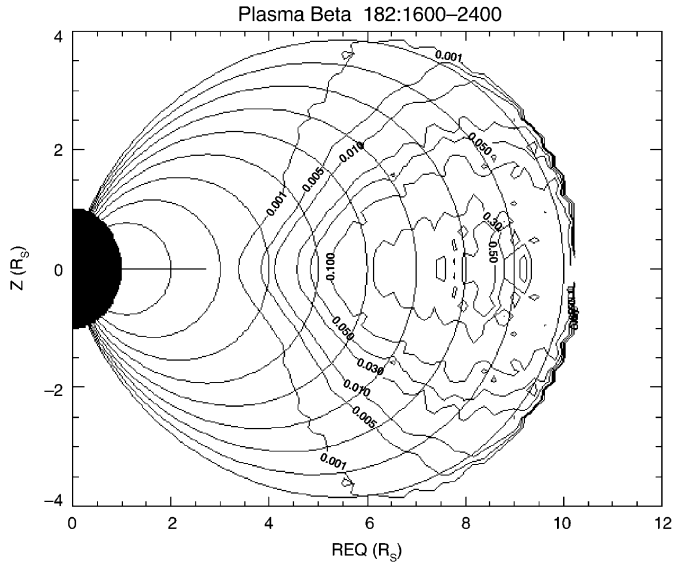

Fig. 8. 2D contour plot of plasma beta as function of equatorial radius R_{EQ} and vertical distance Z for Saturn-centered coordinate system. Dipole field lines are super-imposed.

greater than 1 and the Alfven Mach number can be greater than 1 with peak values near Rhea's L shell. As shown in Sittler et al. (2005), the ring current will be important when $\beta > 1$ or $M_A > 1$ or both are satisfied. The ring current model by Connerney et al. (1983) showed the presence of a ring current confined between $L \sim 8$ and $L \sim 16$, using Voyager magnetometer observations within Saturn's magnetosphere. We must stress, that due to the ring current, the magnetic field lines will be more extended and result in a larger equatorial confinement of the plasma ions due to centrifugal and magnetic mirror forces. This will result in higher plasma β and M_A values near the equator for $L > 8.74$ than estimated here. Therefore, the drop in these values outside $L \sim 8.74$ may not occur and the ring current will extend to $L \sim 16$ as observed by Connerney et al. (1983). Furthermore, there is evidence that the plasmasphere outer boundary was at $L \sim 10$ for SOI period, while it is more typically at $L \sim 15$ (see later discussions). From such 2D maps, one can estimate the ring current corrections, repeat our field-aligned calculations, then calculate the ring current again and repeat this process until convergence occurs. Here, comparisons with magnetometer data will play a critical role in this calculation. As stated above, the Maurice et al. (1997) equations do allow for ring current corrections to be implemented. Eventually, we need to extend our analysis to $L > 15$ and include the pressure contributions of the hot plasma for $E > 50$ keV to provide a more definitive estimate of the plasma pressure. We do note, that Sittler et al. (2006b), using Voyager 1 ring plane crossing observations at Dione's L shell, showed that the ions dominated the plasma pressure and that a majority of the plasma pressure was confined to ion energies $E < 10$ keV. They also showed that the heavy ions dominated the plasma pressure when compared to the protons. The fluid results by Sittler et al. (2005, 2006a), were moment calculations that covered the energy range $1\,\mathrm{V} < E/Q < 50\,\mathrm{kV}$ for the water group ions (but signal was generally not detected for $E/Q > 20$ kV).

2.3. Further evidence for assumed temperature anisotropies of plasma ions and electrons

As discussed in Sittler et al. (2005, 2006a), the ion densities are over-estimated by the ratio $\sqrt{T_\perp/T_\parallel}$ since the instrument's observations were confined to a plane perpendicular to the magnetic field during the Cassini spacecraft SOI approach trajectory. Also, during this same time period, the RPWS instrument measured UHR

emissions as reported in Moncuquet et al. (2005) who used these observations to estimate the local electron density along the spacecraft's trajectory. Using the following expression, one can estimate a correction factor, CF_{W^+} to the assumed temperature anisotropy for water group ions at the spacecraft location:

$$CF_{W^+} = [n_{W^+}(\text{CAPS}; T_\perp/T_{||} = 5)/(n_e(\text{UHR}) - n_{H^+}(\text{CAPS}; T_\perp/T_{||} = 2))]^2, \quad (3)$$

where n_e(UHR) is the UHR estimate of the electron density, $n_{H^+}(\text{CAPS}; (T_\perp/T_\parallel)_{EQ} = 2)$ is the CAPS estimated proton density with assumed equatorial $(T_\perp/T_\parallel)_{H^+} = 2$ and $n_{W^+}(\text{CAPS}; (T_\perp/T_\parallel)_{EQ} = 5)$ is the CAPS estimated W^+ density with assumed equatorial $(T_\perp/T_\parallel)_{W^+} = 5$. By CAPS we mean the fluid parameters presented by Sittler et al. (2006a). We use Eq. (2) to estimate the temperature anisotropies of protons and water group ions at the spacecraft position from the assumed equatorial values. The results are shown in Fig. 10 with error bars. The error bars are dominated by the uncertainty in the absolute calibration of the CAPS IMS geometric factor for protons and water group ions. As can be seen, corrections are less than a factor of 2 in most cases, so that the equatorial temperature anisotropies range between $5 < (T_\perp/T_\parallel)_{W^+} < 10$. This is an independent confirmation of our assumed temperature anisotropies. A more direct approach could be used, but we prefer this iterative approach since it has less scatter and thus more accurate.

Persoon et al. (2006) performed a comprehensive analysis of RPWS electron density estimates derived from observed UHR emissions for ~20 passes through Saturn's inner magnetosphere. From this study they obtained a single ion scale height estimate of the plasmasphere as a function of dipole L with functional relationship $H = (0.047)R_S L^{1.8}$ with Saturn radius $R_S = 60{,}268$. In their analysis they pointed out that they could not exclude the presence of protons for their higher latitude points and did not have sufficient latitude coverage to see protons if present. Using the relationship $H^2 = 2kT_{\parallel,i}/3m_i\Omega^2$ for a single ion plasmasphere and making assumption only due to water group ions, we can derive a relationship for the water group ion temperature anisotropy as follows:

$$(T_\perp/T_{||})_{W^+} = 2kT_{\perp,W^+}(\text{CAPS})/(3m_{W^+}\Omega^2)/[(0.047)R_S L^{1.8}]^2, \quad (4)$$

where $\Omega = V_\phi(\text{CAPS})/R$, V_ϕ(CAPS) is the plasma azimuthal velocity measured by CAPS, m_{W^+} = the mean water group ion mass ≈ 16 − 18 amu measured by CAPS and $T_{\perp,W^+}$(CAPS) is the water group ion perpendicular temperature measured by CAPS. The results are shown in Fig. 11, which shows very little temperature anisotropy at L~10 and gradually increases to $(T_\perp/T_\parallel)_{W^+}$~5.0 at L~3.8. The large rise near L~3.4 is partially due to spacecraft maneuver with IMS only seeing hot ion component with T_{W^+}~100 eV (see Sittler et al., 2005). Furthermore, Persoon et al. (2006) observe a larger-scale height H than used above for $L < 3.8$ and if we used the actual measured scale height we would estimate lower temperature anisotropy for this inner region than that estimated using Eq. (4).

The lower $(T_\perp/T_\parallel)_{W^+}$~1 for $L > 6$ does not necessarily contradict our original assumption that $(T_\perp/T_\parallel)_{W^+}$~5.0 at ring plane for $3.4 < L < 10$. For example, Fig. 2 shows that for L~10, where the spacecraft is at $\lambda \sim -12^\circ$, the protons contribute ~$\frac{1}{2}$ the ion density. As shown in Figs. 2–7, the proton scale height is very large and dominates the ion density at high latitudes. Therefore, the approach by Persoon et al. (2006) will tend to over-estimate the scale height of the water group ions if we assume the water

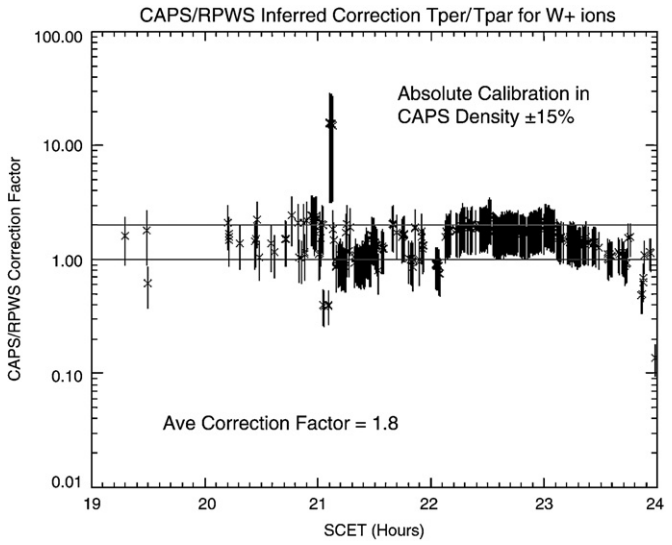

Fig. 10. Plot of CAPS/RPWS correction term for temperature anisotropy $(T_\perp/T_\parallel)_{W^+}$ as function of SCET time. See text for details.

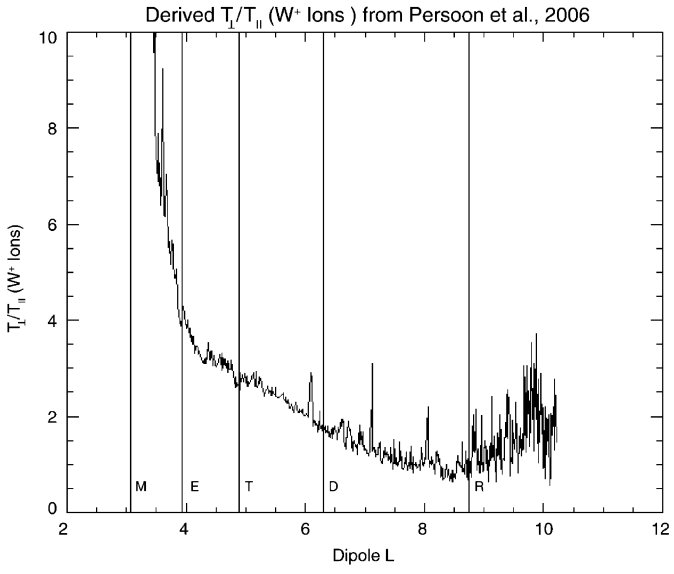

Fig. 11. Plot of derived $(T_\perp/T_\parallel)_{W^+}$ as function of dipole L shell. We used inferred $T_\parallel$ from the RPWS density scale height measurements from Persoon et al. (2006) and the perpendicular measurements $T_\perp$ measured by CAPS and reported by Sittler et al. (2006a). Icy satellite L shells indicated.

group ions dominate the ion density at all observed L, λ values. They did not see evidence of proton contamination since they see no evidence of a change in slope of n_e to less negative values with increasing latitude. We will address this issue below.

Using our 2D map of n_e presented in Fig. 7 and repeating the analysis by Persoon et al. (2006) for all the trajectories used in their study, we can essentially reproduce their results as shown by Fig. 12a–e. In fact, our simulations give the appearance of a larger $(T_{\parallel})_{W+}$ than that estimated by Persoon et al. (2006). For our simulations we added random noise $\sim\pm 20\%$ of the local electron density similar to the variances in the Persoon et al. (2006) data. When we do this, the variations in the simulated data tend to hide any evidence of a change in scale height or slope as one move from low latitude where water group

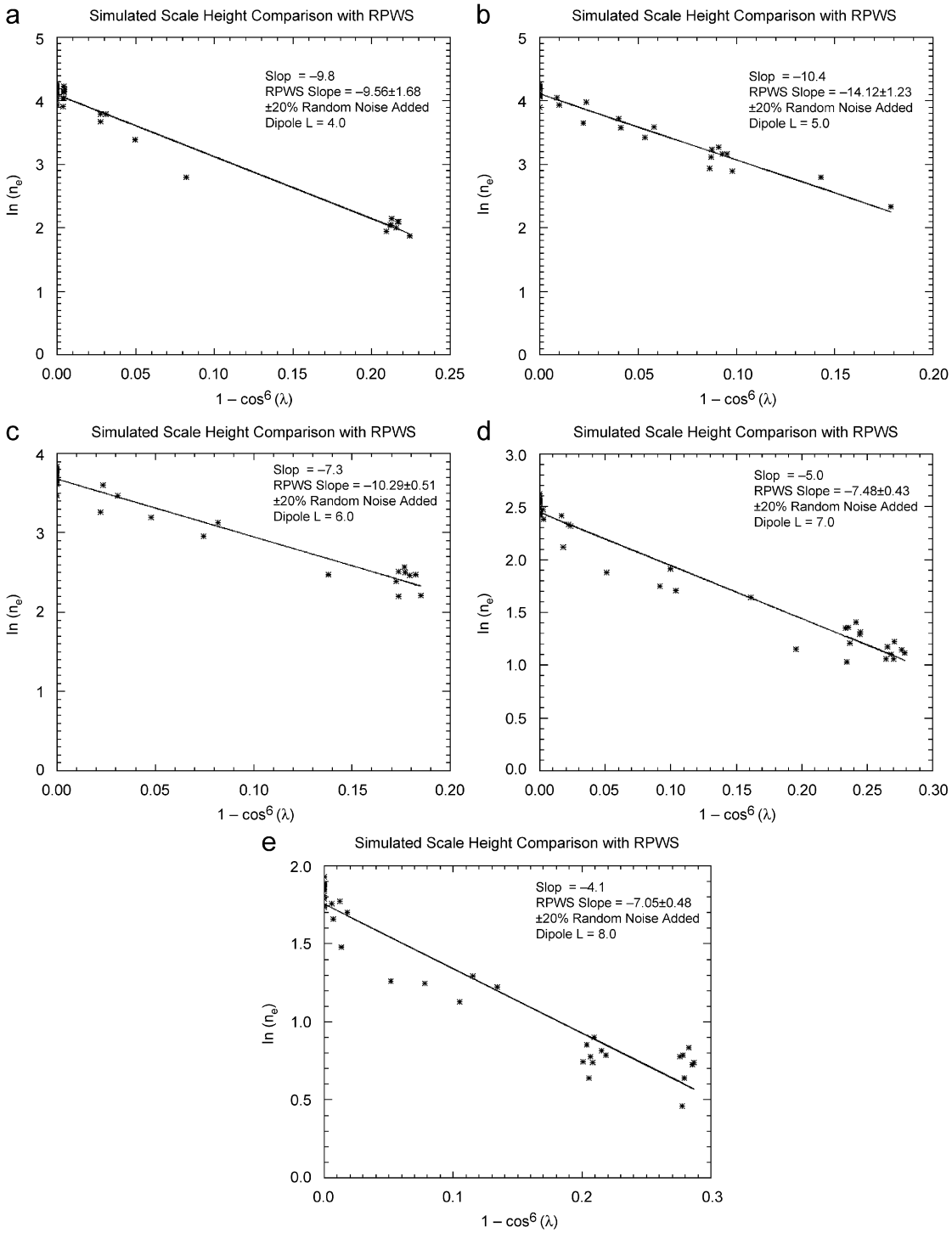

Fig. 12. Plot of simulated variations of $\ln(n_e)$ versus $1-\cos^6\lambda$. Random noise $\sim\pm 20\%$ is super-imposed. Linear fits are done to get measure of single scale height as done by Persoon et al. (2006) who used RPWS electron densities. Fig. 12a–e are for dipole L shells of 4.0, 5.0, 6.0, 7.0 and 8.0, respectively.

ions dominate to higher latitudes where protons dominate. This change in slope is evident if we turn the noise off. Since our simulations infer a larger scale height than that by Persoon et al. (2006), it could indicate that protons are less important at higher latitudes than estimated by our simulations. The distribution of protons with latitude is sensitive to the electron temperature used and its temperature anisotropy. For example, using cold–hot electron components (not yet available), using $(T_\perp/T_\parallel)_e > 1$ and/or using $(T_\perp/T_\parallel)_{H^+} > 2$, may bring our simulations in better agreement with the results by Persoon et al. (2006). The analysis of the CAPS electron observations presented by Rymer et al. (2006) show that the thermal or cold electrons are isotropic, while the hot electron component can be anisotropic. So, the electron temperature anisotropy may not be an important effect for our proton calculations. It is important to note, that both the electrons and protons can be used as an accurate probe of the ambipolar electric field $E_\parallel$. The proton issue is not expected to make an important correction to our results presented here, but will be addressed in a later study.

As another check of our calculations, if our field-aligned solutions are correct, our predicted equatorial electron densities should approximately equal RPWS measured equatorial electron densities from later equatorial orbits within Saturn's inner magnetosphere. This comparison is made in Fig. 13. As can be seen, our predictions are very close to that measured by RPWS inside Rhea's L shell and confirms our assumption that $(T_\perp/T_\parallel)_{W^+} \sim 5.0$ for the water group ions. Between Dione and Rhea our estimates are somewhat lower, but there is evidence that this region is highly turbulent (Sittler et al., 1983; Rymer et al., 2006). Inside Dione's L shell they are within RPWS uncertainties

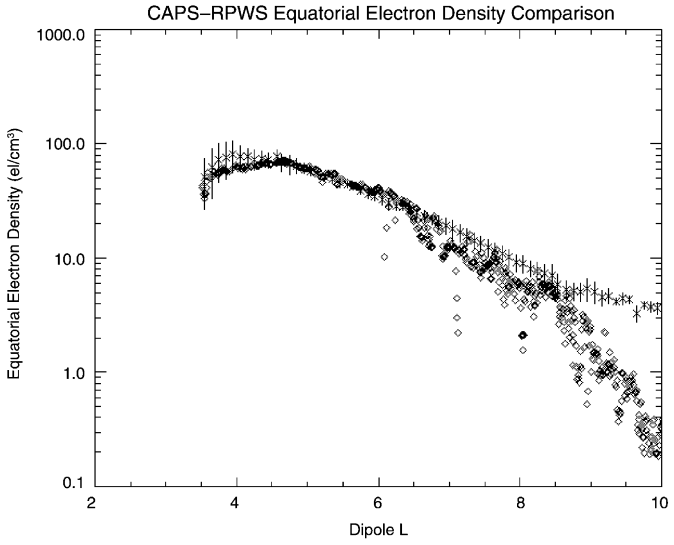

Fig. 13. Here we have plotted equatorial electron densities extrapolated down to the equatorial plane from our 2D model using diamond (◇) symbols and average equatorial electron densities measured by RPWS using asterisk (*) symbols, which have been summed over many equatorial passes of Saturn's inner magnetosphere. For the RPWS densities their one sigma error bars are indicated.

where the plasma is deep within Saturn's magnetosphere and more stable. Outside Rhea's L shell our SOI equatorial densities are much less than the RPWS equatorial densities. Our electron densities for SOI along spacecraft trajectory are in good agreement with RPWS. This discrepancy is probably due to enhanced loss of plasma from the plasmasphere outer boundary during SOI, relative to the later equatorial orbits when the plasmasphere extends to larger radial boundaries. Fig. 13 does confirm that the temperature anisotropy we are using for water groups ions is correct. If one used Fig. 11 as being correct, then our densities would not be consistent with the RPWS UHR estimated densities, as shown in Fig. 10, since the ion geometric factors cannot change in time and space. Fig. 10 could not exclude using $(T_\perp/T_\parallel)_{W^+} \sim 10.0$, but when we compute equatorial densities using this anisotropy for water group ions, one gets a poor comparison with the RPWS equatorial densities, generally greater by factors of 2 inside $L \sim 8$, with exception around $L \sim 4.0$. When we repeated the same exercise for $(T_\perp/T_\parallel)_{W^+} \sim 2.0$, we did get a good match inside $L \sim 8.0$, but when considering Fig. 10 we got total ion densities well above locally measured RPWS electron densities along the Cassini trajectory. Therefore, $(T_\perp/T_\parallel)_{W^+} \sim 5.0$ gives the best representation of all the data sets.

3. Computation of ion total flux tube content $N_{ION}L^2$, ion production S_{ION} and neutral production S_W within Saturn's inner magnetosphere

3.1. Compute ion total flux tube content $N_{ION}L^2$

We need to estimate $N_{ION}L^2$ which is the total number of ions on a dipole L shell. This L shell, under steady state, will extend all around the planet at a particular L value and radial extent $\Delta L \sim 1$. Since the cross-section of the magnetic field goes like $1/B(s)$ with

$$B(s(\theta)) = \frac{B_S}{R_p^3 L^3} \frac{\sqrt{1+3\cos^2\theta}}{\sin^6\theta}, \tag{5}$$

the volume of the flux tube per unit length decreases with increasing latitude and the contribution due to protons, for example, is not as large as one might think from their relatively higher densities at high latitudes as shown in Figs. 2–4. Then using the relation between arc length $s(\theta)$ and θ as shown below:

$$\frac{\partial s}{\partial \theta} = R_p L \sin\theta \sqrt{1+3\cos^2\theta} \tag{6}$$

one gets the integral equation for N_Φ as shown in Eq. (7), which is the total number of ions on a unit flux tube:

$$N_\Phi = 2R_S/B_S L^4 \int_{\theta_m}^{\pi/2} n_{ION}(L,\theta)\sin^7\theta \, d\theta. \tag{7}$$

Therefore, $N_\Phi dL$ is the total number of ions between L and $L + dL$. The factor of 2 is used since the integral only covers, for example, northern latitudes (i.e., co-latitude $\theta = \pi/2 - \lambda$, λ is the latitude). The lower limit of the

integrand, θ_m is the co-latitude point of the field line at Saturn's ionosphere. The $\sin^7\theta$ term is due to the increase in the dipole field strength as one move along the field line to higher latitudes. In order to get the total number of ions on an L shell then we must multiply this expression by $2\pi LR_S\Delta LR_S/\Delta A_\Phi$ where $\Delta A_\Phi = L^3/B_S$ is the area of a unit flux tube in Maxwells at the equator in cm^2 and $B_S = 0.2$ Gauss. Therefore, this factor represents the number of unit flux tubes within an L shell that extends all around the planet. We will call this quantity the number of ions on a unit L shell

$$N_{ION} = 4\pi R_S^3 L^2 \int_{\theta_m}^{\pi/2} n_{ION}(L,\theta)\sin^7\theta\, d\theta. \quad (8)$$

Finally, we get the quantity $N_{ION}L^2$ by multiplying Eq. (8) by L^2

$$N_{ION}L^2 = 4\pi R_S^3 L^4 \int_{\theta_m}^{\pi/2} n_{ION}(L,\theta)\sin^7\theta d\theta \quad (9)$$

which has the same functional relationship as $N_{\underline{\Phi}}$ within a constant factor. This is the expression we used to compute the total flux tube content for protons and water group ions. Since, N_{ION} represents the total number of ions on a unit L shell, it is the quantity to use when estimating the ion production and neutral production rates. $N_{ION}L^2$ is the quantity that is preserved when outward diffusive transport occurs. This follows from the approximation that the plasma remain confined to a flux tube and the magnetic flux is conserved during flux tube interchange motions. We have a plot of $N_{ION}L^2$ in Fig. 14. This figure shows a peak at Dione's L shell where $N_{W^+} \gg N_{H^+}$ in most cases. For $L>8$ $N_{H^+}\sim N_{W^+}$ or larger. This result is similar to that originally found by Richardson and Sittler (1990) and later by Richardson et al. (1998) who found H^+ to be low relative to the heavy ion component which they thought was dominated by O^+. At the time it was thought there was a deficit of H^+ relative to O^+ if the source was dominated by the ionization of water molecules. The Voyager results by Richardson and Sittler (1990) also showed a broader distribution for $N_{ION}L^2$ with no discernable peaks, but did show sharp drop-off inside $L\sim4$.

This apparent discrepancy in protons can be explained by the ion composition data of CAPS originally shown by Young et al. (2005), Tokar et al. (2006) and shown here in Fig. 15 using the latest calibration results of the IMS. These results show that water ions were primarily molecular and that in the vicinity of Enceladus, the hydronium ion H_3O^+ dominates. Then if we use the following expression:

$$<m_{ion}> = <m_{W^+}> + N_{H^+}/N_{W^+} \quad (10)$$

with

$$<m_{W+}> = po*16.0 + poh*17.0 + pw*18.0 + ph3o*19.0, \quad (11)$$

and po, poh, pw and ph3o being the fractional abundance of O^+, OH^+, H_2O^+ and H_3O^+, respectively, for water

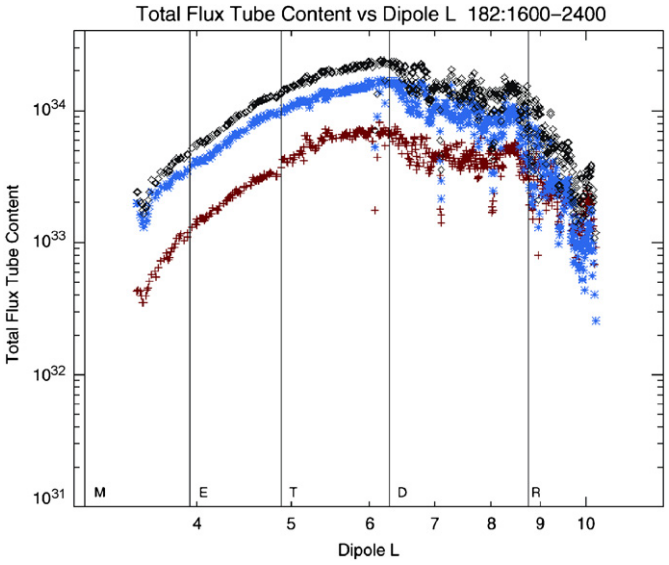

Fig. 14. Total flux tube content for protons, $N_{H^+}L^2$ (red), and for water group ions (blue), $N_{W^+}L^2$, and the sum of protons and water group ions (black) plotted as a function of dipole L. Icy satellite L shells are indicated.

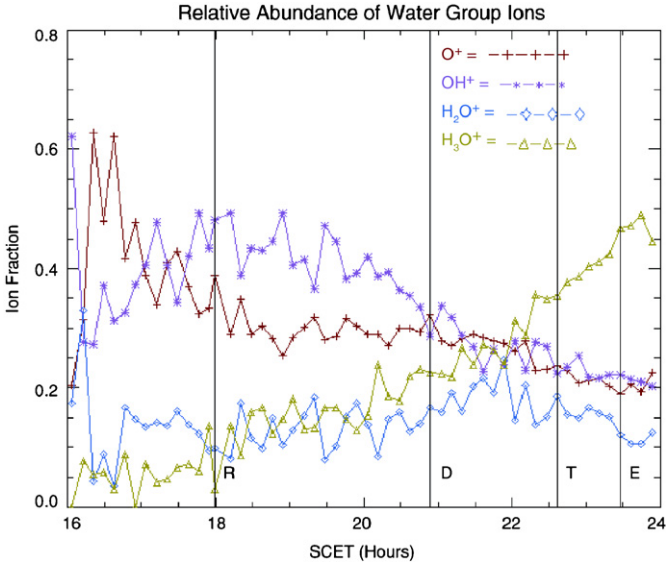

Fig. 15. The relative abundance of the water group ions (O^+, OH^+, H_2O^+ and H_3O^+) plotted as function of time with icy satellite L shells indicated.

group ions as shown in Fig. 15, we can determine if H^+ is under abundant for a water source. The results of this calculation is shown in Fig. 16 where it shows $<m_{ion}> \approx 18.0$ except for the period around $L\sim10$ where protons can dominate. Note, that Eq. (10) uses the total number of ions on a unit L shell, so the results are to first-order independent of how the ions are distributed along field lines. But, since Eq. (11) uses local compositional values of the water fragments and we are at higher latitudes for $L\sim10$, we could be over-estimating the importance of protons at $L\sim10$. Furthermore, from our previous comparison with the RPWS UHR electron densities by

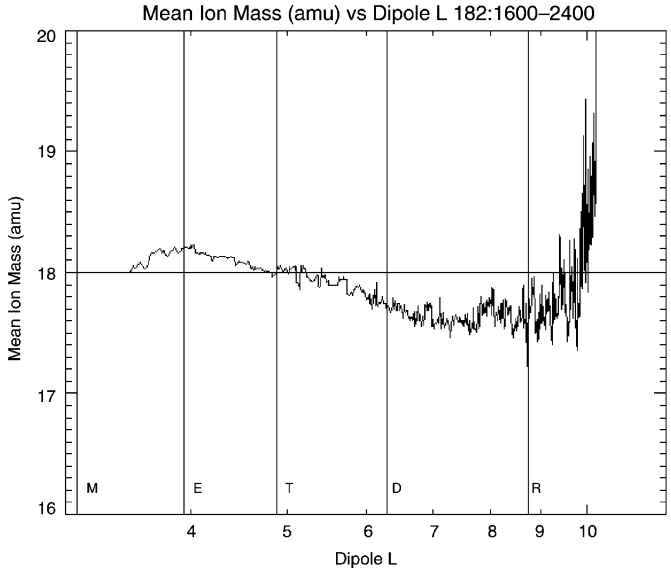

Fig. 16. Mean ion mass in amu, is plotted versus dipole L shell. Icy satellite L shells are indicated. This plot shows that the source molecule has mass~18 amu, and since composition data clearly indicates that the ions are water group ions, the source cloud must be dominated by water molecules.

Persoon et al. (2006), we could be over-estimating the proton densities at higher latitudes in this outer region, so that our results could still be consistent with water clouds being the primary source of ions for L~10. Therefore, within experimental uncertainties, our results are consistent with water molecules being the dominant source of ions for Saturn's inner magnetosphere and with most of the hydrogen ions locked up in the molecular water ions and there is no deficit of H^+ ions as originally thought (Richardson and Sittler, 1990).

3.2. Compute ion production rate S_{ION} as function of dipole L

The fundamental equation governing the transport of plasma within Saturn's magnetosphere, while also accounting for its various sources $S_{\rm ION}$ and loss terms $L_{\rm ION}$ is given by the radial diffusion equation

$$\frac{\partial}{\partial L}\left[\frac{D_{LL}}{L^2}\frac{\partial(N_{\rm ION}L^2)}{\partial L}\right]+S_{\rm ION}-L_{\rm ION}=0 \tag{12}$$

as originally derived by Dungey (1965). We will not solve this equation here, but is shown in order to see how the various terms interact and how the diffusion coefficient D_{LL} provides radial transport. One can estimate the time scale for radial transport using Eq. (12) as derived in Cheng (1986) under the condition of no sources and sinks as follows:

$$\frac{\partial}{\partial L}\left[\frac{D_{LL}}{L^2}\frac{\partial(N_{\rm ION}L^2)}{\partial L}\right]=-\frac{N_{\rm ION}}{\tau_D}. \tag{13}$$

Siscoe and Summers (1981) derived an explicit expressions for D_{LL} in the case of centrifugally driven radial transport. The diffusion coefficient, which is normally parameterized as $D_{LL}=KL^m$ with m~3, is shown to be proportional to the mass-loading rate. In our case, we use a characteristic radial transport time scale $\tau_D\approx 1/D_{LL}=\tau_{D_0}(L_0/L)^3$ to provide a local time scale for ion loss via radial transport. We use a characteristic time scale τ_{D_0}~5 days at Dione's L shell, $L_0=6.3$, from Richardson et al. (1998) for our model calculations presented here.

The recent results by Sittler et al. (2006a) showed observational evidence for convective radial transport super-imposed on radial diffusive transport. In the paper by Andre et al. (2006), they have made detailed correlations of magnetic field fluctuations with respect to the fluid velocity fluctuations from Sittler et al. (2006a), which includes the radial velocity component $V_{\rm R}$. The correlations are consistent with flux tube inter-change motions and give support to the radial velocities and azimuthal velocities estimated by Sittler et al. (2006a). If the results by Sittler et al. (2006a) are correct, then Eq. (12) will also need convective terms in addition to radial diffusion terms. The convective transport could also be due to non-linear effects in the centrifugally driven radial diffusion coefficient as derived by Siscoe and Summers (1981) which is $\propto {\rm d}NL^2/{\rm d}L$. At Dione's L shell $V_{\rm R}$~2 km/s, which for transport over ΔL~1 gives residence time τ_D~3×10^4 s or 8–9 h which is 14 times faster than that estimated by Richardson et al. (1998) τ_D~5 days at same L shell. If so, the magnetosphere is an order of magnitude more dynamic than originally thought and ion production an order of magnitude larger than estimated here in the vicinity of Dione's L shell. It could also be true, that transport is outward for longitudes sampled by Cassini during SOI approach and inward at other longitudes. Then residence time scales could be longer. Finally, the radial diffusion equation will be used when a more comprehensive analysis of our results is provided.

In order to estimate the ion production rate we use the following expression:

$$\frac{{\rm d}S_{\rm ION}}{{\rm d}L}=N_{\rm ION}/\tau_{\rm Loss}=\frac{N_{\rm W^+}}{\tau_{\rm W^+,Loss}}+\frac{N_{\rm H^+}}{\tau_{\rm H^+,Loss}}, \tag{14}$$

for which we have assumed steady state with $\tau_{\rm Loss}$ representing the characteristic loss time scale of ions due to radial transport τ_D and recombination $\tau_{\rm REC}$. Note, that in Eq. (8) for $N_{\rm ION}$ we have retained ΔL term, which was previously set to 1, divided both sides of Eq. (14) by ΔL and then took the differential limit as $\Delta L->{\rm d}L$. One can then integrate this expression over ΔL to get the local ion production. One usually sets $\Delta L=1$. Charge exchange is not used, since it does not produce or remove ions from the system. Protons, H^+, could charge exchange with water molecules or water group ions, W^+, could charge exchange with hydrogen atoms and produce protons, etc. Therefore, we combine all neutral atoms and molecules as a single species with $N=N_{\rm H}+N_{\rm O}+N_{\rm OH}+N_{\rm H_2O}$, along with the assumption that the original source of neutrals is water molecules. Furthermore, the neutral clouds will be confined

near the ring plane where the ion composition is dominated by water group ions (i.e., small correction due to protons). The loss time scale can be expressed as

$$\frac{1}{\tau_{\rm Loss}} = \frac{1}{\tau_D} + \frac{1}{\tau_{\rm REC}} \tag{15}$$

with $\tau_D = \tau_{D_0}/(L/L_0)^3$ as described above. $\tau_{\rm REC}$ symbolizes the time scale for recombination which will be important for molecular ions such as OH^+, H_2O^+, and H_3O^+. This will especially be true in the vicinity of Enceladus where the electrons are relatively cold, $T_{\rm ec}\sim 1$ eV, and molecules dominate (Young et al., 2005) and shown in Fig. 15 above. For atomic ions such as H^+ and O^+ recombination is negligible. We estimate the time scale for recombination by performing the volume integral of the recombination rate coefficient weighted by the ion density, say for water group ions, along a flux tube. We then divide this integral by the volume integral of the ion density along a flux tube to get a weighted mean of $1/\tau_{\rm REC}$. In order to compute this quantity correctly, we use the relative abundances of O^+, OH^+, H_2O^+ and H_3O^+ shown in Fig. 15. We then sum up the various contributions as follows:

$$\frac{1}{\tau_{\rm REC}} = \sum_{j=1}^{5} \frac{1}{\tau_{{\rm REC},j}} = \frac{\sum_j \int n_j(s(\theta)) v_{{\rm REC},j}(s(\theta)) \sin^7\theta \, {\rm d}\theta}{\sum_j \int n_j(s(\theta)) \sin^7\theta \, {\rm d}\theta}, \tag{16}$$

with $j = 1$–5 for H^+, O^+, OH^+, H_2O^+ and H_3O^+ ions. The recombination rate $v_{{\rm REC},j}(s(\theta))$ is a function of electron density $n_e(s(\theta))$ and thermal electron temperature $T_{\rm ec}(s(\theta))$ which are both a function of co-latitude θ along dipole L shells. In the case of protons and atomic oxygen ions, recombination time scales are very long, and transport dominates. The transport and ion recombination time scales as a function of dipole L are shown in Fig. 17. This figure shows recombination dominating inside Dione's L shell and transport dominating outside Dione's L shell.

The ion production $S_{\rm ION}$ for water group ions and protons added together, using Eqs. (14)–(16), is shown in Fig. 18. The ion production $S_{\rm ION}\sim 10^{27}$ ions/s shows a very broad radial dependence with peaks at Tethys and Dione. The peak near Rhea's L shell will probably be coincident with Rhea when one takes into account ring current corrections. We see no peak at Enceladus' L shell.

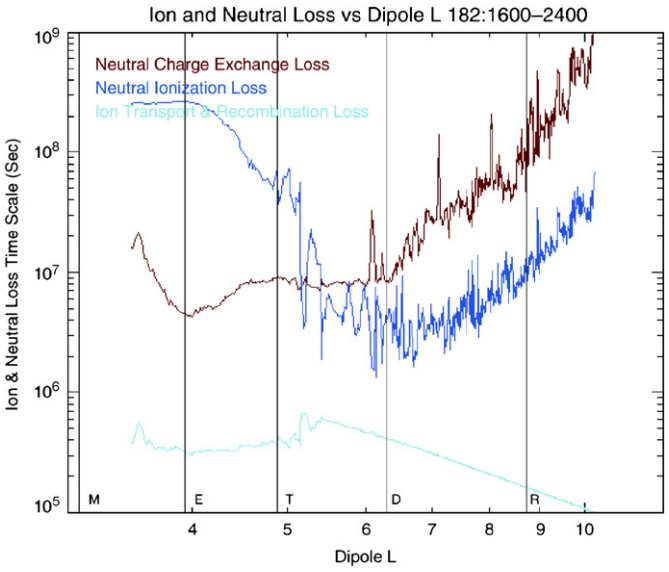

Fig. 17. Ion and neutral loss time scales plotted versus dipole L shell. Icy satellite L shells are indicated. We used the neutral cloud model in Johnson et al. (2006) and Burger et al. (2007). Neutral charge exchange loss time scale indicated in red, neutral ionization loss time scale indicated in blue and ion transport plus ion recombination loss time scale indicated in turquoise.

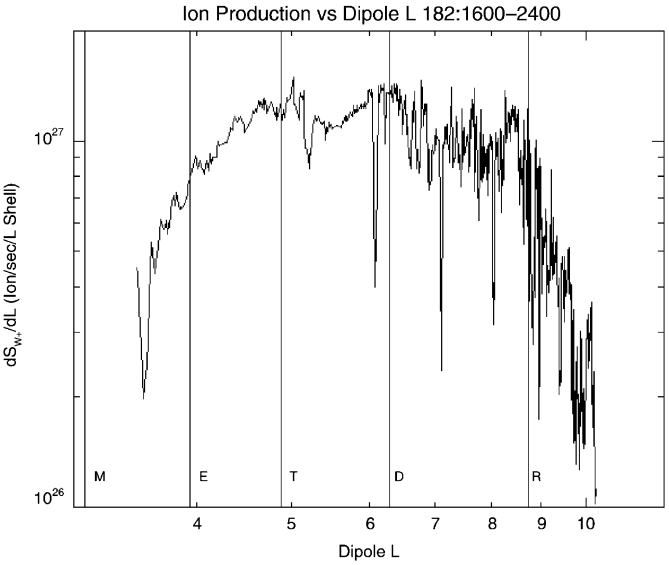

Fig. 18. Plot of ion production per unit L shell versus dipole L. Icy satellite L shells are indicated. The plot shows peaks near Tethys, Dione and Rhea L shells.

3.3. Compute neutral production of water molecules S_W as function of dipole L

In order to estimate the neutral production rate, we need to know the ionization loss time scale for neutrals $\tau_{\rm ION}$ and the charge exchange loss time scale for neutrals $\tau_{\rm CH}$, in addition to the ion loss time scale $\tau_{\rm Loss}$ presented in the previous section. We estimate these time scales similar to that in Eq. (16), except we weighted the integrals by an assumed neutral cloud model and then divided by the flux tube integral of the neutral cloud model. We then get

$$\frac{1}{\tau_{\rm ION}} = \sum_{j=1}^{3} \frac{1}{\tau_{{\rm ION},j}} = \frac{\sum_j \int n_j(s(\theta)) v_{{\rm ION},j}(s(\theta)) \sin^7\theta \, {\rm d}\theta}{\sum_j \int n_j(s(\theta)) \sin^7\theta \, {\rm d}\theta}, \tag{17}$$

for which we used neutral clouds [O], [OH], and [H_2O] for $j = 1$–3. For charge exchange we used the expression

$$\frac{1}{\tau_{\rm ICH}} = \sum_{j=1}^{3} \frac{1}{\tau_{{\rm ICH},j}} = \frac{\sum_j \int n_j(s(\theta)) v_{{\rm ICH},j}(s(\theta)) \sin^7\theta \, {\rm d}\theta}{\sum_j \int n_j(s(\theta)) \sin^7\theta \, {\rm d}\theta}, \tag{18}$$

with neutral clouds [H], [O], [OH] and [H_2O] for $j = 1$–4 used. For each index j, for example, we would perform the integral for say, [OH], times the appropriate charge exchange rate parameter over a unit flux tube and then divide this integral by the volume integral of just the neutral density over a unit flux tube. The above integrals are evaluated using the neutral cloud model by Johnson et al. (2006), which includes the Enceladus torus and the OH torus. For [H] and [O] we use the neutral cloud model by Richardson et al. (1998). This neutral cloud model, shown in Fig. 19, shows a large spike at Enceladus' L shell. For comparison, we have super-imposed the Richardson et al. (1998) neutral cloud model on top of that for Johnson et al. (2006). The expression we use for each neutral component is

$$n_j(\theta) = n_{EQ,j} \exp(-((1 - \cos^6\theta) L R_S / H_j^2)). \quad (19)$$

For the OH component of the neutral cloud originally determined from HST observations by Richardson et al. (1998) we used the scale height $H_j \sim 0.45 R_S$. For the water cloud due to Enceladus modeled by Johnson et al. (2006) the scale height $H_j \sim 0.1 R_S$ or less and was variable with dipole L. Most of the reaction rates for charge exchange, electron impact ionization and photoionization can be found in Sittler et al. (2004) Tables 1–3 or Burger et al. (2007). An exception is the electron impact ionization rates for water molecules where we have used the review article by Itikawa and Mason (2005). The charge exchange reaction rates are a function of the relative velocity between ions and neutrals and are proportional to the ion density. Both can vary along dipole field lines. Ions tend to co-rotate with the planet, while neutrals follow Keplarian velocities. These affects are taken into account by our calculations, where we do neglect corrections due to finite thermal speeds of both neutral and ion VDF. This is a fairly good approximation since Sittler et al. (2005, 2006a) found the sonic Mach number for both protons and water group ions to be ~2.0. The electron ionization rates are functions of the electron temperature and electron density, for which we have used the total electron temperature shown in Fig. 1 and the total electron density $n_e = n_{H^+} + n_{W^+}$, respectively.

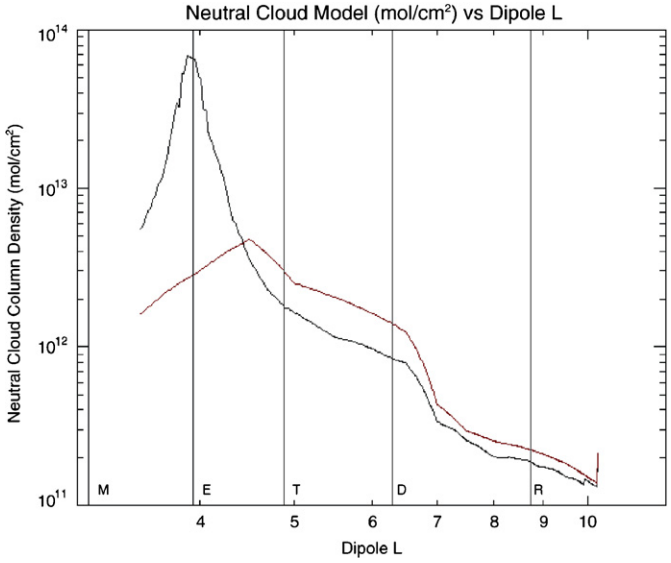

Fig. 19. Vertical neutral cloud column density by Johnson et al. (2006) and Burger et al. (2007) plotted as function of dipole L shell. Here we see dominant peak centered on Enceladus' L shell. We have also super-imposed the vertical neutral cloud column density by Richardson et al. (1998) in red for purposes of comparison. Outside of Tethys the Richardson et al. (1998) column densities are higher due to fact that Johnson et al. (2006) model gives lower water densities in this outer region and those by Richardson et al. (1998) are derived from OH cloud measurements, Voyager plasma measurements and model calculations.

Fig. 17 shows a plot of all the relevant time scales. Inside of Enceladus' L shell the ionization time scale saturates at $\tau_{ION} \sim 10^8$ s which is just photoionization. In this region the electrons are so cold $T_{ec} \sim 1$ eV, electron impact ionization is extremely small. The time scale is slightly shorter due to a minor hot electron component as noted above.

In order to estimate the neutral production rate we first use the following relationship:

$$\frac{N_W}{\tau_{ION}} \sim \frac{N_{W^+}}{\tau_{Loss}}. \quad (20)$$

In steady state, this equation assumes the rate of ionization of water neutrals within a unit L shell, is equal to the loss of water ions within the same unit L shell. As argued above, charge exchange does not contribute to ion production and that most of the ions close to the equatorial plane where the neutrals are located, is dominated by water group ions. This expression allows us to estimate N_W

$$N_W \sim N_{W^+}(\tau_{ION}/\tau_{Loss}). \quad (21)$$

In steady state the neutral production is given by the following expression:

$$\frac{dS_W}{dL} \sim N_W \left(\frac{1}{\tau_{ION}} + \frac{1}{\tau_{CH}}\right). \quad (22)$$

We then substitute Eq. (21) into Eq. (22) and we finally get

$$\frac{dS_W}{dL} \sim \frac{N_{W^+}}{\tau_{Loss}} \left[\frac{\tau_{ION}}{\tau_{CH}} + 1\right]. \quad (23)$$

As can be seen, except for our estimate of the indicated time scales in Eq. (23), we can compute the production rate for neutrals without detailed knowledge of the neutral populations. As for the ion production, we retained the ΔL term and took the differential limit in Eqs. (22–23). We did have to use the radial transport time scale estimated by Richardson et al. (1998), but in the vicinity of Enceladus, Fig. 17 shows that recombination dominates, so that the estimate of S_W within the inner magnetosphere is not sensitive to the ion transport rate. Eq. (23) shows that the neutral production is boosted by the short recombination time scales within the inner magnetosphere where molecular water ions dominate. Fig. 17 also shows that the charge exchange time scale has a significant localized minimum at Enceladus' L shell. This results in a localized

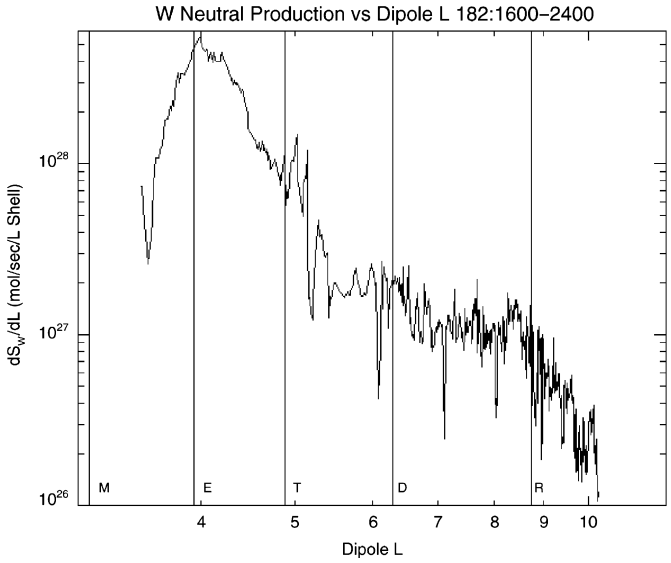

Fig. 20. Neutral production rate per unit L shell plotted versus dipole L shell. Icy satellite L shells are indicated. We used the neutral cloud model in Johnson et al. (2006) and Burger et al. (2007). It shows large peak centered on the L shell of Enceladus with total source $S_W \sim 2 \times 10^{28}$ mol/s.

maximum in the ratio of $\tau_{ION}/\tau_{CH} \gg 1$ at Enceladus, which will further boost the neutral production at Enceladus. A plot of Eq. (23) is shown in Fig. 20.

As expected from our previous discussion, Fig. 20 shows a large peak $dS_W/dL \sim 3 \times 10^{28}$ mol/s, which is centered on Enceladus' L shell. If, we integrate the results in Fig. 20 at $L \sim 4.0$ and $\Delta L \sim 1$, we estimate the large-scale neutral production rate $S_W \sim 2 \times 10^{28}$ mol/s. As stated previously, our calculations are correct to within a factor of 2 in an absolute sense.

4. Discussion and conclusions

One of the main science objectives of the CAPS instrument is to measure the distribution and composition of the plasma within Saturn's magnetosphere, to measure the sources and sinks of plasma and neutrals, and to study the transport, dynamics and energetics of the plasma within Saturn's magnetosphere. The papers by Sittler et al. (2005, 2006a) defined the fluid and compositional properties of the plasma along the SOI approach trajectory and set the stage for this paper to define the 2D distribution of the plasma within Saturn's inner magnetosphere. From our 2D maps of proton density, water group ion density and electron density we were able to compute the total flux tube content $N_{ION}L^2$ as a function of dipole L for protons and water group ions. Then by knowing the lifetime of ions against recombination and transport, one was able to compute the ion production, S_{ION}, as a function of dipole L. We then used this information plus the timescale for loss of neutrals due to charge exchange reactions, electron impact ionization and photoionization, to compute the production of neutrals within Saturn's inner magnetosphere as a function of dipole L. This latter step was done using the neutral cloud model by Johnson et al. (2006). The neutral production showed a broad peak near Enceladus' L shell with source strengths $S_W \sim 2 \times 10^{28}$ mol/s. Therefore, our model calculations provide an independent estimate of the neutrals being poured into Saturn's magnetosphere by Enceladus as the likely source. Our estimates are very close to those by Jurac and Richardson (2005) based on HST data, by Johnson et al. (2006) who reproduced the HST cloud from a south polar Enceladus source of $S_W \sim 10^{28}$ mol/s, by Hansen et al. (2006) who used UVIS stellar occultation measurements to estimate $S_W \sim 0.5$–1×10^{28} mol/s and the modeling of the plumes detected by Cassini by Burger et al. (2007). $S_W \sim 0.8$–1.0×10^{28} mol/s, who combined the observations by ISS, UVIS, INMS and CAPS. Here we note that Enceladus may have contributions to the smaller neutral production rates at Tethys, Dione and Rhea due to low energy charge transfer collisions at the Enceladus torus as discussed by Johnson et al. (2006) who was able to explain the OH cloud using this mechanism and shown in Fig. 19. Therefore, one must consider this correction when estimating the neutral and ion production rates for these other icy satellites.

In the earlier works by Richardson and Sittler (1990), and Richardson et al. (1998), it was thought that atomic ions (H^+, O^+) dominated the plasma composition and recombination was thought to be less important. Richardson and Sittler (1990) estimated total flux tube content $N_{O^+}L^2 \sim 10^{34}$ ions and $N_{H^+}L^2 \sim 5 \times 10^{33}$ ions, while here we found peak values $N_{W^+}L^2 \sim 3 \times 10^{34}$ ions and $N_{H^+}L^2 \sim 5 \times 10^{33}$ ions. The model results by Richardson and Sittler (1990) found a flat variation of NL^2 with dipole L from $L = 4$ to $L = 12$ with sharp drop inside of Enceladus' L shell. In our case we see a broad peak centered on Dione's L shell. But, in a qualitative sense their results are equivalent. Furthermore, the equatorial densities displayed in Richardson and Sittler (1990) and Richardson et al. (1998) are very similar with ours, but are closer to the results of Persoon et al. (2005, 2006) than ours for $L \sim 8$–10 where we expect the plasma to be more time dependent, Sittler et al. (1983) and Rymer et al. (2006). As shown in Eqs. (14) and (23), Richardson et al. (1998) would tend to underestimate the ion production and neutral production within Saturn's inner magnetosphere where they found neutral production rates peaking at $S_W \sim 10^{27}$ mol/s. More recently, Jurac and Richardson (2005) revised their original estimates with neutral production near Enceladus' L shell to $S_W \sim 10^{28}$ mol/s. Here, they used a Monte Carlo calculation for neutrals and ions and solved both populations in a more self-consistent manner. In their model they use a source rate of neutrals from the icy moons as a free parameter in their model calculations and do not say how the neutrals are emitted from the icy moons. This more recent result did have more molecular water group ions in their calculations which resulted in higher neutral production rates as discussed here. The composition results by Young et al. (2005) and those presented here are supportive

of their calculations, but their model calculations did not include hydronium ions (H_3O^+) which turned out to be dominant at Enceladus. Ip (2000) did consider the composition issues of water molecular ions within the inner magnetosphere and showed that water molecular ions, including the hydronium ion, could result if neutral densities in the vicinity of Enceladus exceeded 10^4 mol/cm^3. Ip also discussed the importance of radial transport rates, which if faster resulted in more molecular water ions relative to atomic O^+. If transport rates were low, then recombination via electron impact, $T_e \sim 1$ eV, would deplete the plasma of molecular ions.

We have compared our 2D maps of electron density with the RPWS electron densities by Persoon et al. (2005, 2006) and have shown them to be consistent within experimental errors. These comparisons, three in all, confirm usage of a nominal equatorial temperature anisotropy $(T_\perp/T_\parallel)_{W^+} \sim 5$ for water group ions and confirms the accuracy of our 2D maps. We also assumed $(T_\perp/T_\parallel)_{H^+} \sim 2$ and $(T_\perp/T_\parallel)_e \sim 1$ for protons and electrons, respectively. Since $T_{H^+} \sim T_{ec}$, the proton distribution along field lines is sensitive to the ambipolar electric field and thus the electron temperature and its temperature anisotropy. Our comparisons with RPWS electron densities do favor larger anisotropies for both protons and electrons. This will be a subject for future work, since we can use protons to probe the ambipolar electric field.

Our 2D maps have many future applications, such as the calculation of wave propagation within the magnetosphere, making 2D maps of plasma beta and Alfven Mach number, estimating the magnetosphere's stability against various MHD modes such as centrifugally driven flux tube interchange motions, and the trajectories of charged dust particles within Saturn's magnetosphere, just to name a few.

The results presented in this paper, lay the ground work for future work. We discuss several possibilities here. First, we need improve our 2D mapping of plasma populations by directly integrating CAPS moments, RPWS electron densities, hot plasma parameters from MIMI and magnetic field observations, into a common set of force balance equations. These calculations will include corrections due to the ring current first identified by Connerney et al. (1981) to be confined between 8 and $15R_S$ within Saturn's magnetosphere. We extend this study to include equatorial and non-equatorial orbits with good compositional information. Our 2D maps we based on the approximation that the ions were well described by bi-Maxwellian velocity distributions. Other possibilities are Kappa distributions and partially filled shell distributions. So, work in this area needs investigation.

Secondly, we need to study the radial distribution of plasma sources by a full resolution of the transport equations. We need to study transport model(s), relevance of radial diffusion approach and correct diffusion coefficient(s) in the different regimes of transport. The results by Sittler et al. (2006a) indicate that outward convective transport is super-imposed onto diffusive transport and convective terms may need to be added to the transport equations. The observed radial velocities indicate that Saturn's magnetosphere is much more dynamic and time dependent than originally thought. Using the 2D distributions one can study the stability of the magnetosphere against centrifugally driven flux tube inter-change motions and is this a non-linear process (i.e., radial diffusion coefficient a function of the mass-loading rate).

Thirdly, we need to couple the transport model to a full neutral cloud production, transport and loss model. Initial attempts in this area have been made by Richardson et al. (1998) and Jurac and Richardson (2005) using Voyager plasma observations. But future models will include the more comprehensive Cassini observations, inclusion of ring current corrections, consideration of non-bi-Maxwellian VDF, measurements of ion temperature anisotropies, ion composition measurements and more comprehensive fluid parameters over many orbits (low and high inclination) around Saturn.

References

Andre, N., Sittler Jr., E.C., Thomsen, M.F., Rymer, A.M., Blanc, M., Burch, J.L., Coates, A.J., Crary, F.J., Goldstein, J., Khurana, K.K., Krupp, N., Kurth, W.S., Leisner, J.S., Louarn, P., Mauk, B.H., Persoon, A.M., Russell, C.T., Dougherty, M.K., Gurnett, D.A., Krimigis, S.M., Mitchell, D.G., Young, D.T., 2006. Plasma transport signatures at Saturn 1. Observational evidence during Cassini inbound orbit insertion. J. Geophys. Res., in review.

Brown, R.H., Clark, R.N., Buratti, B.J., Cruikshank, D.P., Barnes, J.W., Mastrapa, R.M.E., Bauer, J., Newman, S., Momary, T., Baines, K.H., Bellucci, G., Capaccioni, F., Cerroni, P., Combes, M., Coradini, A., Drossart, V., Formisano, R., Jaumann, Y., Langevin, D.L., Matson, T.B., McCord, P., Nelson, R.M., Nicholson, P.D., Sicardy, B., Sotin, C., 2006. Composition and physical properties of Enceladus' surface. Science 311, 1425–1428.

Burger, M.H., Sittler, E.C., Johnson, R.E., Smith, H.T., Tucker, O.J., Shematovich, V.I., 2007. Understanding the escape of water from Enceladus. J. Geophys. Res. 112, A06219, doi:10.1029/2006JA012086.

Cheng, A.F., 1986. Radial diffusion and ion partitioning in the Io torus. Geophys. Res. Lett. 13, 517–520.

Connerney, J.E.P., Acuna, M.H., Ness, N.F., 1981. Saturn's ring current and inner magnetosphere. Nature 292, 724.

Connerney, J.E.P., Acuna, M.H., Ness, N.F., 1983. Currents in Saturn's magnetosphere. J. Geophys. Res. 88, 8779.

Dougherty, M.K., Khurana, K.K., Neubauer, F.M., Russell, C.T., Saur, J., Leisner, J.S., Burton, M.E., 2006. Identification of a dynamic atmosphere at Enceladus with the Cassini magnetometer. Science 311, 1406–1409.

Dungey, J.W., 1965. Effects of the electromagnetic perturbations on particles trapped in the radiation belts. Space Sci. Rev. 4, 199–222.

Hansen, C.J., Esposito, L., Stewart, A.I.F., Colwell, J., Hendrix, A., Pryor, W., Shemansky, D., West, R., 2006. Enceladus' water vapor plume. Science 311, 1422–1425.

Huang, T.S., Birmingham, T.J., 1992. The polarization electric field and its effect in an anisotropic magnetospheric rotating plasma. J. Geophys. Res. 97, 1511–1519.

Ip, W.-H., 2000. Thermal plasma composition in Saturn's magnetosphere. Planet. Space Sci. 48, 775.

Itikawa, Y., Mason, N., 2005. Cross sections for electron collisions with water molecules. J. Phys. Chem. Ref. Data 34 (1), 1–22.

Johnson, R.E., Smith, H.T., Tucker, O.J., Liu, M., Burger, M.H., Sittler Jr., E.C., Tokar, R.L., 2006. The Enceladus and OH Tori at Saturn. Astrophys. J. Lett. 644, L137–L139.

Jones, G.H., Roussos, E., Krupp, N., Paranicas, C., Woch, J., Lagg, A., Mitchell, D.G., Krimigis, S.M., Dougherty, M.K., 2006. Enceladus' varying imprint on the magnetosphere of Saturn. Science 311, 1412–1415.

Jurac, S., Richardson, J.D., 2005. A self-consistent model of plasma and neutrals at Saturn: neutral cloud morphology. J. Geophys. Res. 110, A09220.

Maurice, S., Blanc, M., Prange, R., Sittler Jr., E.C., 1997. The magnetic-field-aligned polarization electric field and its effect on particle distribution in the magnetospheres of Jupiter and Saturn. Planet Space Sci. 45, 1449–1465.

Moncuquet, M., Lecacheux, N., Meyer-Vernet, N., Cecconi, B., Kuth, W.S., 2005. Quasi-thermal noise spectroscopy in the inner magnetosphere of Saturn with Cassini/RPWS: electron temperatures and densities. Geophys. Res. Lett. 32, L20S02.

Persoon, A.M., Gurnett, D.A., Kurth, W.S., Hospodarsky, G.B., Groene, J.B., Canu, P., Dougherty, M.K., 2005. Equatorial electron density measurements in Saturn's inner magnetosphere. Geophys. Res. Lett. 32, L23105.

Persoon, A.M., Gurnett, D.A., Kurth, W.S., Groene, J.B., 2006. A simple scale height model of the electron density in Saturn's plasma disk. Geophys. Res. Lett. 33, L18106.

Porco, C.C., Helfenstein, P., Ingersoll, P.C., Wisdom, J., West, R., Neukum, G., Denk, T., Wagner, R., Roatsch, T., Kieffer, S., Turtle, E., McEwen, A., Johnson, T.V., Rathbun, J., Veverka, J., Wilson, D., Perry, J., Spitale, J., Brahic, A., Burns, J.A., DelGenio, A.D., Dones, L., Murray, C.D., Squyres, S., 2006. Cassini observes the active south pole of Enceladus. Science 311, 1393–1401.

Richardson, J.D., 1986. Thermal ions at Saturn: plasma parameters and implications. J. Geophys. Res. 91, 1381–1389.

Richardson, J.D., Sittler Jr., E.C., 1990. A plasma density model for Saturn based on Voyager observations. J. Geophys. Res. 95, 12019–12031.

Richardson, J.D., Eviatar, A., McGrath, M.A., Vasyliunas, V.M., 1998. OH in Saturn's magnetosphere: observations and implications. J. Geophys. Res. 103, 20245–20255.

Rymer, A.M., Mauk, B.H., Hill, T.W., Paranicus, C., Andre, N., Sittler Jr., E.C., Mitchell, D.G., Smith, H.T., Johnson, R.E., Coates, A.J., Young, D.T., Bolton, S.J., Thomsen, M.F., Dougherty, M.K., 2006. Electron sources in Saturn's magnetosphere. J. Geophys. Res. 112 (A2), A02201.

Shemansky, D.E., Matheson, P., Hall, D.T., Hu, H.-Y., Tripp, T.M., 1993. Detection of the hydroxyl radical in the Saturn magnetosphere. Nature 363, 329–331.

Siscoe, G.L., Summers, D., 1981. Centrifugally driven diffusion of iogenic plasma. J. Geophys. Res. 86, 8471–8479.

Sittler Jr., E.C., Ogilvie, K.W., Scudder, J.D., 1983. Survey of low-energy plasma electrons in Saturn's magnetosphere. J. Geophys. Res. 88, 8848–8870.

Sittler Jr., E.C., Johnson, R.E., Jurac, S., Richardson, J.D., McGrath, M., Crary, F., Young, D.T., Nordholt, J.E., 2004. Pickup ions at Dione and Enceladus: Cassini plasma spectrometer simulations. J. Geophys. Res. 109, A02104.

Sittler Jr., E.C., Thomsen, M., Chornay, D., Shappirio, M.D., Simpson, D., Johnson, R.E., Smith, H.T., Coates, A.J., Rymer, A.M., Crary, F., McComas, D.J., Young, D.T., Reisenfeld, D., Dougherty, M., Andre, N., 2005. Preliminary results on Saturn's inner plasmasphere as observed by Cassini: comparison with Voyager. Geophys. Res. Lett. 32 (14), L14S04.

Sittler Jr., E.C., Thomsen, M., Johnson, R.E., Hartle, R.E., Burger, M., Chornay, D., Shappirio, M.D., Simpson, D., Smith, H.T., Coates, A.J., Rymer, A.M., McComas, D.J., Young, D.T., Reisenfeld, D., Dougherty, M., Andre, N., 2006a. Cassini observations of Saturn's inner plasmasphere: Saturn orbit insertion results. Planet. Space Sci. 54, 1197–1210.

Sittler Jr., E.C., Johnson, R.E., Smith, H.T., Richardson, J.D., Jurac, S., Moore, M., Cooper, J.F., Mauk, B.H., Michael, M., Paranicas, C., Armstrong, T.P., Tsurutani, B., 2006b. Energetic nitrogen ions within the inner magnetosphere of Saturn. J. Geophys. Res. 111, A09223.

Spahn, F., Schmidt, J., Albers, N., Horning, M., Makuch, M., Seiβ, M., Kempf, S., Srama, R., Dikarev, V., Helfert, S., Moragas-Klostermeyer, G., Krivov, A.V., Sremcevic, M., Tuzzolino, A.J., Economou, T., Grun, E., 2006. Cassini dust measurements at Enceladus and implications for the origin of the E ring. Science 311, 1416–1418.

Spencer, J.R., Pearl, J.C., Segura, M., Flasar, F.M., Mamoutkine, A., Romani, P., Buratti, B.J., Hendrix, A.R., Spilker, L.J., Lopes, R.M.C., 2006. Cassini encounters Enceladus: background and the discovery of a south polar hot spot. Science 311, 1401–1405.

Tokar, R.L., Johnson, R.E., Hill, T.W., Pontius, D.H., Kurth, W.S., Crary, F.J., Young, D.T., Thomsen, M.F., Reisenfeld, D.B., Coates, A.J., Lewis, G.R., Sittler Jr., E.C., Gurnett, D.A., 2006. The interaction of the atmosphere of Enceladus with Saturn's plasma. Science 311, 1409–1412.

Waite, J.H., Combi, M.R., Ip, W.-H., Cravens, T.E., McNutt Jr., R.L., Kasprzak, W., Yelle, R., Luhmann, J., Niemann, H., Gell, D., Magee, B., Fletcher, G., Lunine, J., Tseng, W.-L., 2006. Cassini ion and neutral mass spectrometer: Enceladus plume composition and structure. Science 311, 1419–1422.

Young, D.T., Berthelier, J.-J., Blanc, M., Burch, J.L., Bolton, S., Coates, A.J., Crary, F.J., Dunlop, M.W., Goldstein, R., Grande, M., Hill, T.W., Johnson, R.E., Baragiola, R.A., Kelha, V., McComas, D.J., Mursula, K., Sittler, E.C., Svenes, K.R., Szegö, K., Tanskanen, P., Thomsen, M.F., Bakshi, S., Barraclough, B.L., Bebesi, Z., Delapp, D., Dunlop, M.W., Gosling, J.T., Furman, J.D., Gilbert, L.K., Glenn, D., Holmlund, C., Illiano, J.-M., Lewis, G.R., Linder, D.R., Maurice, S., McAndrews, H.J., Narheim, B.T., Pallier, E., Reisenfeld, D., Rymer, A.M., Smith, H.T., Tokar, R.L., Vilppola, J., Zinsmeyer, C., 2005. Composition and dynamics of plasma in Saturn's magnetosphere. Science 307, 1262–1266.